Eur. Phys. J. B **29**, 377–384 (2002)
DOI: 10.1140/epjb/e2002-00321-8

THE EUROPEAN PHYSICAL JOURNAL B

CEF nature of the magnetic excitations in ordered $HoNi_2B_2C$

N. Cavadini[1,a], Th. Strässle[1], P. Allenspach[1], P.C. Canfield[2], and Ph. Bourges[3]

[1] Laboratory for Neutron Scattering, ETH Zürich & Paul Scherrer Institut, 5232 Villigen PSI, Switzerland
[2] Ames Laboratory, Department of Physics and Astronomy, Iowa State University, Ames, Iowa 50011, USA
[3] Laboratoire Léon Brillouin, CEA/CNRS-Saclay, 91191 Gif-sur-Yvette, France

Received 25 February 2002 / Received in final form 13 May 2002
Published online 14 October 2002 –

Abstract. The magnetic excitations in the antiferromagnetic phase of $HoNi_2B_2C$ are studied by inelastic neutron scattering on single crystals for the first time. Spectra measured at constant $T = 2$ K along symmetry directions of the reciprocal space are well explained in terms of crystal electric field (CEF) magnetic excitons within the $J = 8$ ground state multiplet of Ho^{3+}. Very modest bandwidth with planar energy dispersion describes the magnetic exciton dynamics. A perturbative model approach consisting of the CEF states in the effective exchange mean-field provides a simple but applicable characterization of the experimental observations. The microscopic determination of the relevant exchange parameters is discussed in connection with previous works on the subject.

PACS. 74.70.Dd Ternary, quaternary and multinary compounds – 75.10.Dg Crystal-field theory and spin Hamiltonians – 78.70.Nx Neutron inelastic scattering

1 Introduction

Unconventional superconductors are compounds where the occurrence of the superconducting state overcomes the classical model framework. Rare-earth borocarbides RNi_2B_2C are regarded as unconventional superconductors on their own right, since superconductivity coexists and competes with long-range antiferromagnetic order on a comparable temperature scale in R = Ho, Dy, Er and Tm. Of the above the R = Ho case is of particular interest due to the rich phase diagram summarized in reference [1]. Whereas it is widely accepted that the magnetic properties of $HoNi_2B_2C$ involve the trivalent Ho^{3+} sites only, the details of the interaction between the resulting $J = 8$ moments are far from being settled. These are governed by the interplay of CEF splitting and exchange interactions, putting the basis of theoretical approaches as detailed in Section 2. Estimates of the relevant model parameters are available from magnetization, susceptibility and specific heat measurements, but the detailed understanding of the Ho-Ho interactions certainly relies on inelastic neutron scattering (INS) investigations, which access the evolution of the magnetic states throughout the (Q, ω) space. Unfortunately, the presently available microscopic characterizations of $HoNi_2B_2C$ are limited to *powder averaged* INS studies – an experimental drawback which afflicts all representatives of the RNi_2B_2C family. This note provides the first account of comprehensive *single crystal* INS studies of the magnetic excitation spectra in $HoNi_2B_2C$. For the above reasons the results to be addressed in the following not only decidedly improve the description of the title compound, but also contribute to the understanding of the whole family of rare-earth borocarbides.

Particular attention is devoted to the microscopic discussion of the neutron spectrum observed at $T = 2$ K in the ordered antiferromagnetic (AF) phase of $HoNi_2B_2C$. In Section 2, previous experimental and theoretical characterizations of the magnetic properties in $HoNi_2B_2C$ are briefly summarized. In Section 3, the sample preparation and INS measurements are described. Very modest and anisotropic energy dispersion characterizes the experimental observations. In Section 4 the discussion of the results is thoroughly developed within a self-consistent mean-field CEF model approach. In Section 5 comments and outlooks are provided in a broader framework. In the Appendix further details of the model calculations are given for the reader's convenience.

2 Magnetism

$HoNi_2B_2C$ crystallizes in the tetragonal space group I4/mmm, with parameters summarized in references [2,3]. The space group is modestly distorted by magnetorestriction in the ordered AF phase, to be addressed below. The magnetic properties originate from the trivalent Ho^{3+} sites located at the corners and in the center of the nuclear unit cell. Comprehensive magnetization and specific heat investigations are reported in reference [4].

[a] e-mail: nordal.cavadini@psi.ch

They indicate the importance of CEF induced single ion anisotropy within the $J = 8$ ground state multiplet of Ho^{3+}. The low-lying tetragonal CEF scheme consists of a singlet, a doublet and a singlet, well separated from higher levels as quantitatively discussed in reference [5]. INS investigations in the paramagnetic phase of the title compound refined the complete tetragonal CEF scheme by fits to the energy and intensity of the powder averaged neutron spectra, see reference [6]. The resulting CEF parameters were further shown to be in agreement with static measurements, see reference [6]. The above work provides reference quantities for the modeling of the INS experimental observations in the ordered antiferromagnetic phase, to which we adhere in the following of this contribution. Below $T \sim 8$ K, $HoNi_2B_2C$ undergoes two successive incommensurate magnetic phase transitions before entering at $T_N \sim 5$ K a commensurate AF phase described by the propagation wave vector $q_{AF} = (0, 0, 1)$ in reciprocal lattice units (r.l.u.), see references [7–9]. The commensurate AF phase with moments along the $[1, 1, 0]$ direction is explained on the basis of single ion anisotropy of CEF character and well reproduced by a mean-field CEF approach developed in reference [6]. The angular dependence of the field-induced magnetization unambiguously certifies the above assignment, see reference [10].

The elementary CEF energy levels of Ho^{3+} in the AF phase are characteristically renormalized against the paramagnetic phase. The exchange mean-field $B_{MF} \parallel [1, 1, 0]$ accounting for this renormalization is estimated as 2.5 T-3.0 T according to references [6,11]. This quantity expresses the microscopic interaction

$$H_{MF} = -\left(g\mu_B B_{MF}\right) J = -\left(\langle J\rangle \ \tilde{J}(q_{AF})\right) J \qquad (1)$$

where $\langle J\rangle = 8$ denotes the staggered moment in units of the ground multiplet, $\tilde{J}(q_{AF})$ the Fourier transform (FT) of the exchange interactions $\tilde{J}_{ij}$ between the rare-earth sites at q_{AF} and J the irreducible spin operator. The remaining notation in equation (1) has the usual meaning. Less is known regarding the strength and nature of the distinct $\tilde{J}_{ij}$ contributing to the exchange interactions. From a CEF based Curie-Weiss interpretation of the susceptibility measurements, ferromagnetic exchange in the planes and antiferromagnetic exchange between the planes is reported, in agreement with the underlying magnetic structure, see reference [5]. The exchange is strongly planar according to the dominant contribution determined in the same. INS investigations in diluted powder samples provide first quantitative approximates of the Ho-Ho exchange interactions under consideration of effective cluster interactions, reference [12]. Magneto-restriction is further reported from the structural studies in the ordered AF phase, see references [13,14]. The tetragonal (I4/mmm) to orthorhombic (Fmmm) distortion along the $[1, 1, 0]$ direction is quantified as 0.19% in reference [13]. Estimates from a point charge model described in the Appendix demonstrate that the modest symmetry lowering does not markedly affect the tetragonal CEF scheme of Ho^{3+}.

A complete theoretical approach for the magnetic ground state based on the CEF states is discussed in references [15,16], with model parametrization from the bulk experimental results. A further theoretical approach within a semi-classical exchange model is presented in reference [17]. Both models well reproduce the $M(T, H)$ boundaries between the different metamagnetic phases experimentally observed *along* the $[0, 0, 1]$ direction, fail however to account for the metamagnetic phases *perpendicular* to the $[0, 0, 1]$ direction recently evidenced from static investigations by neutron diffraction in references [18,19]. In the cited works the phases perpendicular to $[0, 0, 1]$ reported at $T = 2$ K at finite external fields are ascribed to the incommensurability common throughout the borocarbides at the nesting wave vectors, see reference [20]. The results presented in the following provide the first direct dynamic investigations of the exchange interactions in $HoNi_2B_2C$ by neutron spectroscopy. Among other issues to be discussed, the energy dispersion of the CEF magnetic excitons at $T = 2$ K is clearly anisotropic and evidences a broad incommensurate minimum in the plane perpendicular to $[0, 0, 1]$, supporting the above and confirming the need for further theoretical efforts. At the same time, it provides a valuable reference to organize future experimental studies.

3 Experiment

Isotopically substituted $HoNi_2^{11}B_2C$ single crystals of sufficient size for the present investigation were prepared by a high temperature flux-growth technique described in reference [21]. The crystal shape was plaquette-like, with the plaquette face perpendicular to the $[0, 0, 1]$ direction. The quality of the samples was tested by bulk magnetization as a function of temperature and external field, and found to well reproduce the known $M(T, H)$ phase diagram. For the purpose of the INS investigations to follow, several crystals were mounted on a common aluminum plate to obtain a total sample mass of the order of 3 g. The alignment of the single crystals in the $[1, 1, 0], [0, 0, 1]$ scattering plane was performed piecewise by the conventional two-axis modus. The mosaicity of the total sample was obtained as 2.5 deg from the measured FWHM of the rocking scans at the Bragg reflections.

The INS measurements were performed on the DrüchaL and TASP spectrometers installed at the Spallation Neutron Source SINQ, Villigen PSI and on the 4F2 spectrometer at the Laboratoire Léon Brillouin (LLB), CEA/Saclay. Instruments were operated at fixed final energies $E_f = 3.5$ meV, $E_f = 4.7$ meV and $E_f = 5.0$ meV, respectively, in their standard focusing conditions with open geometry after the sample. Horizontal incoming beam collimation corresponded to $40'$, $40'$ and $60'$, respectively. A cold beryllium filter in front of the analyzer was used in all measurements to suppress higher order contaminations. The sample environment with fixed temperature $T = 2$ K was adopted.

The measurements devoted to the investigation of the CEF magnetic excitons in the AF phase of $HoNi_2^{11}B_2C$ at $T = 2$ K were organized according to the expectations developed in the Appendix. Inclusion of the exchange

Table 1. Renormalized CEF transitions calculated for the $J = 8$ ground state multiplet of Ho^{3+} according to an RPA model presented in Section 3. The list is restricted to the energy range of interest for the present investigation. Δ, $M^{\perp}$ and $M^{||}$ denote the energy (in meV), the planar and the longitudinal transition matrix elements, respectively, at fixed $B_{mf} = 3.0$ T. σ^2 gives the estimated variance on the reference values after the tolerances of the paramagnetic CEF parameters, notation and details of the calculation in the text.

	Δ	$M^{\perp}$	$M^{||}$	$\sigma^2\Delta$	$\sigma^2 M^{\perp}$	$\sigma^2 M^{||}$
$\Gamma_4 \rightarrow \Gamma_5(1)$	1.719	0.23	0.03	0.007^2	0.20^2	0.02^2
$\Gamma_4 \rightarrow \Gamma_5(2)$	1.736	0.14	0.00	0.011^2	0.13^2	0.00^2
$\Gamma_4 \rightarrow \Gamma_1$	3.473	0.00	0.00	0.012^2	0.00^2	0.00^2
$\Gamma_4 \rightarrow \Gamma_2$	12.22	1.30	3.04	0.80^2	0.47^2	1.03^2
$\Gamma_4 \rightarrow \Gamma_5(1)$	13.14	0.02	0.00	0.97^2	0.05^2	0.18^2
$\Gamma_4 \rightarrow \Gamma_5(2)$	13.48	0.26	0.13	0.99^2	0.37^2	0.87^2
$\Gamma_4 \rightarrow \Gamma_3$	14.17	0.02	0.24	1.00^2	0.10^2	0.21^2
...	...			...		

mean-field in the paramagnetic CEF Hamiltonian of Ho^{3+} provides simple but applicable model expectations as follows. Major CEF transitions in the experimentally accessible range are expected for $B_{MF} = 3.0$ T at $E = 1.7$ meV, around $E = 12.2$ meV and around $E = 13.5$ meV. According to the mean-field CEF model these energies correspond to the renormalized $\Gamma_5(1,2), \Gamma_2$ and $\Gamma_5(2)$ states above the Γ_4 ground state, listed in Table 1 after the notation of reference [6]. With the exception of the low-lying $\Gamma_4 \rightarrow \Gamma_5(1,2)$ singlet-doublet transition, the higher $\Gamma_4 \rightarrow \Gamma_2, \Gamma_4 \rightarrow \Gamma_5(2)$ transitions are nondegenerate singlet-singlet transitions. As addressed in the Appendix and presented in Table 1, tolerances in the experimental determination of the starting CEF parameters differently affect the model expectations at finite $B_{MF} = 3.0$ T, which are almost sharp for the low-lying singlet-doublet transition but far less precise for the higher singlet-singlet transitions.

The observed neutron spectra up to $E = 14$ meV confirm the separation of the relevant CEF excited states into a nearly degenerate low-lying doublet state and two higher singlet states. At each wave vector, profiles are reproduced by Gaussian peaks on top of a common background resulting from an overall fit procedure. Within instrumental accuracy, resolution limited peaks are observed for the higher singlet-singlet transitions. This is not valid for the low-lying singlet-doublet transition, which is broader than the instrumental resolution but well explained assuming a minute doublet splitting. The mean energies extracted from the fit procedure detailed in Section 4 correspond to $E = 1.72(1)$ meV, $E = 11.71(2)$ meV and $E = 13.06(2)$ meV, with the doublet splitting of the former corresponding to 0.18(1) meV. The assignments of the CEF transitions are unambiguous with respect to the expectations summarized in Table 1. The mean energy of the low-lying doublet state sharply reflects the model expectation at $B_{MF} = 3.0$ T, thus providing a reliable indicator for the strength of the exchange mean-field. Furthermore, the energy of the higher singlet states are well within the according variances as explained in the Appendix. The mean-field estimate is backed by the energy dispersion discussed in the following, the origin of the doublet splitting is separately discussed in Section 4.

The spectral weight of the distinct CEF transitions is calculated within the same mean-field CEF model approach, with dominant contribution expected from the renormalized $\Gamma_4 \rightarrow \Gamma_2$ transition (Tab. 1). Remarkably, only the renormalized $\Gamma_4 \rightarrow \Gamma_2$ transition shows resolvable energy dispersion limited to the plane perpendicular to the $[0, 0, 1]$ direction. As will be demonstrated, this fact is in quantitative agreement with a perturbative approach based on the CEF states.

A complete quantitative comparison of the experimental results with the theoretical expectations is postponed to Section 4. Here the framework of the adopted Random Phase Approximation (RPA) model is presented in its simplest form, justified by the above observations. Neglecting correlations between the planes, we summarize in the following the expectations elaborated in the Appendix.

The RPA modeling of the interacting CEF states expects a dispersive behavior of the elementary excitations around the mean-field CEF energy scheme, according to the formula

$$E_i^{\alpha\alpha}(q) = \Delta_i - M_i^{\alpha\alpha}\tilde{J}(q), \qquad M_i^{\alpha\alpha} = |\langle\Gamma_i|J^{\alpha}|\Gamma_4\rangle|^2 \quad (2)$$

where the index i distinguishes the CEF transitions, $\alpha = \{x, y, z\}$ denotes the spin coordinate and J^α the irreducible spin operator within the Ho^{3+} ground state multiplet. Γ_i and Γ_4 stays for the renormalized CEF excited and ground state, respectively. The calculation of the according transition energy $\Delta_i = E_i - E_4$ has been anticipated in the text. Equation (2) implies that the dispersive behavior of each magnetic exciton around Δ_i is scaled by the according matrix element M_i. The latter is solely determined by the involved renormalized CEF states, but explicitly dependent on the strength of the internal mean field B_{MF}, *i.e.* $M_i = M_i(B_{MF})$. In turn, B_{MF} reflects $\tilde{J}(q_{AF})$ as addressed in equation (1). From INS measurements on single crystals, the self-consistent determination of $\tilde{J}(q_{AF})$ is thus possible on the basis of the observed magnetic exciton bandwidth around the CEF transition energy. The dominant tetragonal site symmetry justifies a further simplification of equation (2) in planar and axial terms with respect to the [0,0,1] direction. Denoting with $E_i^\perp$ and $E_i^\parallel$ the corresponding energy expectations, the resulting inelastic neutron cross section reads

$$I_i^{\perp,||}(Q,\omega) \sim |f(Q)|^2 \left(1 \pm \frac{Q^z Q^z}{Q^2}\right) M_i^{\perp,||} \delta\left(\hbar\omega - E_i^{\perp,||}(Q)\right) \tag{3}$$

where $f(Q)$ is the form factor of the Ho^{3+} ion, Q^z the projection of the wave vector along $[0, 0, 1]$, $M_i^\perp = M_i^{xx} = M_i^{yy}$, $M_i^{||} = M_i^{zz}$ from the above. The sum and difference of the projection in equation (3) applies to the planar and axial term, respectively, according to the geometrical prefactor in equation (11). We stress at this point that the expressions in equations (2, 3) are justified for non-degenerate transitions, and that for each transition terms mixing different polarizations are neglected in the diagonalization of the RPA equation, see Appendix. Moreover, linearization of the resulting energy dispersion is performed under the assumption of a dominating mean-field CEF energy scheme with respect to the dynamic exchange interactions. Though certainly subject to some idealization, as it will be demonstrated equation (3) provides an applicable description of the experimental observations. Further details are given in the Appendix, calculated energies and transition matrix elements along the above line are summarized in Table 1.

4 Discussion

The quantitative discussion of the INS observations is organized separately for the higher $\Gamma_4 \rightarrow \Gamma_2$, $\Gamma_4 \rightarrow \Gamma_5(2)$ transitions and for the low-lying $\Gamma_4 \rightarrow \Gamma_5(1,2)$ transition, see Table 1. For both groups the emphasis is put on the energy dispersion accessed at wave vectors along different symmetry directions of the reciprocal space. Experimental observations are shown to be well reproduced by the simple model expectations introduced in the previous section.

Spectra of the higher $\Gamma_4 \rightarrow \Gamma_2$, $\Gamma_4 \rightarrow \Gamma_5(2)$ CEF transitions at $T = 2$ K were taken on the TASP spectrometer in the configuration detailed in Section 3. According to Table 1, the $\Gamma_4 \rightarrow \Gamma_2$ transition dominates the spectral weight and the dispersive behavior, following the model discussion. The global fit procedure adopted for the analysis of the profiles features at each wave vector two Gaussian peaks on top of a common background. The FWHM of the peaks is overall fixed at the calculated instrumental energy resolution ΔE, uniquely determined from the instrumental set-up following standard procedures. Excellent account for the observations is claimed from the calculation both inelastically and elastically. The latter was separately tested against the measured incoherent elastic vanadium line. Data sets consisting of the $[h, h, 0], [0, 0, l], [0.5, 0.5, l]$ and $[1, 1, l]$ directions are fitted following the above. The global fit quality further improves fixing the energy of the weaker $\Gamma_4 \rightarrow \Gamma_5(2)$ transition. Results from the dominant $\Gamma_4 \rightarrow \Gamma_2$ transition show unambiguous dispersion of the order $\sim$0.1 meV, almost limited to the plane perpendicular to $[0, 0, 1]$. In Figure 1, a summary of the latter is presented. The energy dispersion according to equation (3) is evaluated for the purpose of the present discussion with $M = 1/3\ (2M^\perp + M^\parallel)$ to be explained below. In Figure 1, the continuous line corresponds to the harmonic *ansatz* $\tilde{J}(q) = 2\tilde{J}_1 (\cos(2\pi q_h) + \cos(2\pi q_k))$ restricted to the $[0, 0, l], [0.5, 0.5, l]$ and $[1.0, 1.0, l]$ directions, with $\Delta = 11.71(2), M\tilde{J}_1 = 0.015(2)$. It is now demonstrated that the above is compatible with the expected exchange mean-field, considering

$$M\tilde{J}(q_{AF}) = M4\tilde{J}_1 = 0.060(8) \text{ meV} \tag{4}$$

with $q_{AF} = (0, 0, 1)$ r.l.u. as introduced in equation (1). Equating the experimental observations in equation (4) to the self-consistent mean-field condition for $B_{mf} = 3.0$ T $\rightarrow \tilde{J}(q_{AF}) = 0.027$ meV as in the Appendix, the experimental estimate $M = 2.2(3)$ is extracted. This estimate compares well with the model calculation for the $\Gamma_4 \rightarrow \Gamma_2$ CEF transition summarized in Table 1, stressing the validity of the above description. The planar exchange interaction $4\tilde{J}_1$ in equation (4) is ferromagnetic and in the same range reported in the static study of the susceptibility, see reference [5]. An undoubted advantage of neutron scattering on single crystals is the wave vector selectiveness of this information. Data along the $[h, h, 0]$ direction indicate that the planar dispersion is better reproduced with the inclusion of next-nearest neighbor interactions. In Figure 1, the dashed line corresponds to the fit obtained under consideration of the $\tilde{J}_2$ and $\tilde{J}_3$ terms in the Appendix, equation (9) with $M\tilde{J}_2 = -M\tilde{J}_3 = 0.026(4)$ meV while retaining the above. Though the discussion of the complete exchange interaction scheme is beyond the scope of this contribution, the experimental results provide direct evidence of a broad minimum at incommensurate position perpendicular to the $[0, 0, 1]$ direction, as anticipated. The alignment of the single crystals unfortunately prevented the collection of experimental data along the $[h, 0, 0]$ direction, see also references [18–20]. In consideration of the variance on the calculated transition matrix elements from Table 1, an

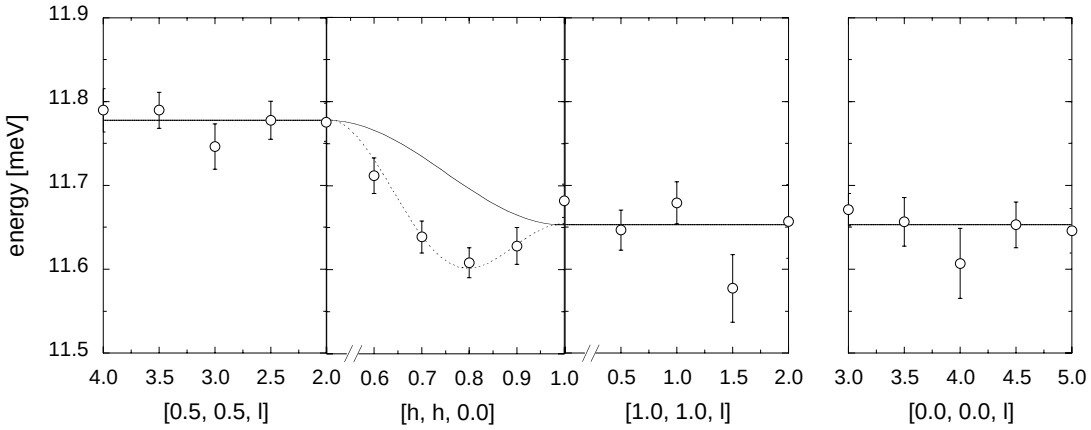

Fig. 1. Energy dispersion of the $\Gamma_4 \rightarrow \Gamma_2$ CEF transition observed in $HoNi_2^{11}B_2C$ single crystals at fixed $T = 2$ K. Symbols correspond to the global fit procedure explained in Section 4, arranged according to the different $[h, h, l]$ directions in reciprocal lattice units. Continuous and dashed lines reproduce the dynamic model expectations from an RPA model including nearest neighbor and next-nearest neighbor planar interactions, respectively.

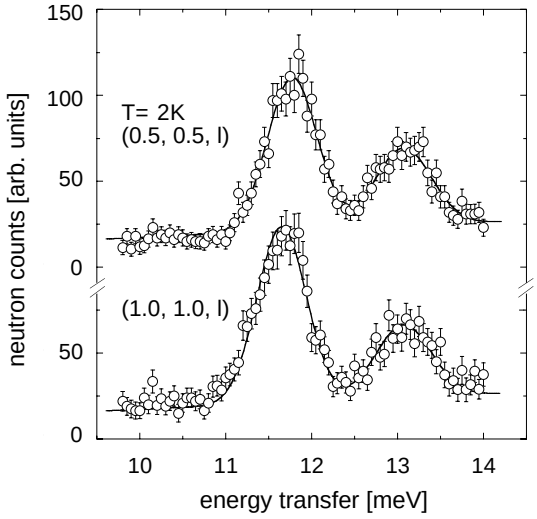

Fig. 2. Neutron profiles of the higher $\Gamma_4 \rightarrow \Gamma_2$, $\Gamma_4 \rightarrow \Gamma_5(2)$ CEF transitions observed in $HoNi_2^{11}B_2C$ single crystals as explained below, fixed $T = 2$ K (TASP, SINQ PSI). Distinct measurements at $\delta l = \{0.0, 0.5, 1.0, 1.5\}$ r.l.u. are merged for $(0.5, 0.5, 2.0 + \delta l)$ r.l.u. (upper panel) and $(1.0, 1.0, \delta l)$ r.l.u. (lower panel). The global fit procedure and the physical observables are addressed in Section 4. Notice the minute energy shift of the dominant transition, according to Figure 1.

averaged matrix element M is assumed in equation (4). This is a robust approximation well supported by the experimental outcomes, see in particular the energy data along $[0, 0, l]$ and $[1, 1, l]$, and justified by the mixed nature of the CEF transition. A discussion of the according spectral weights is presented in the following.

In Figure 2, high statistics profiles collected for $Q = (h, h, l)$ r.l.u. at fixed h but different l values are merged as indicated. The FWHM of the merged profiles is excellently reproduced by the instrumental resolution calculations with no free parameters. These profiles fully justify the neglect of exchange interactions parallel to $[0, 0, 1]$, which are clearly beyond the instrumental capability. Whereas the energy of the weaker $\Gamma_4 \rightarrow \Gamma_5(2)$ transition is fixed as already addressed, unambiguous dispersion of the dominant $\Gamma_4 \rightarrow \Gamma_2$ transition is apparent comparing top and bottom panel, which are vertically displaced for convenience. The organization of the data according to the model expectations in equation (3) further shows that the calculated matrix elements are in satisfactory agreement with the observed spectral weights, taking as an input the CEF scheme from reference [6]. Global fits of the energy integrated intensity from the same points as in Figure 1 are performed according to

$$I^{\perp} + I^{||} = |f(Q)|^2 \left[\left(1 + \frac{Q^z Q^z}{Q^2} \right) M^{\perp} + \left(1 - \frac{Q^z Q^z}{Q^2} \right) M^{||} \right] \quad (5)$$

with $M^{\perp}$ and $M^{||}$ as only free parameter. Relative polarizations $M^{||} : M^{\perp}$ thus determined correspond to 2.31(40) and 2.97(1.05) for the $\Gamma_4 \rightarrow \Gamma_2$ and for $\Gamma_4 \rightarrow \Gamma_5(2)$ transition, respectively. From the averaged $M = 1/3\,(2M^{\perp} + M^{||})$ the ratio between the weights of the $\Gamma_4 \rightarrow \Gamma_2$ and $\Gamma_4 \rightarrow \Gamma_5(2)$ transitions is obtained as 2.55(67). These spectral weights confirm the assignments of the CEF states within the variances reported in Table 1. The experimental evidence of the mixed polarization nature of the higher transitions justifies *a posteriori* the energy fit with the averaged M as presented for the $\Gamma_4 \rightarrow \Gamma_2$ transition. Furthermore, the ratio between the weights of the $\Gamma_4 \rightarrow \Gamma_2$ and $\Gamma_4 \rightarrow \Gamma_5(2)$ transitions supports the much smaller dispersion postulated for the latter from equation (2) and accordingly neglected on grounds of the instrumental limitations.

We now comment on the behavior of the low-lying $\Gamma_4 \rightarrow \Gamma_5(1, 2)$ CEF transition. The investigations were performed on the DrüchaL and 4F2 spectrometer in the configurations detailed in Section 3. Following the same theoretical approach, almost vanishing dispersive behavior is expected around the calculated CEF transition energy. However, a complication arises here due to the doublet

nature of the excited state. At each wave vector experimental profiles were fitted assuming two nearly degenerate, resolution limited Gaussian peaks following the global procedure already explained. Data were overall well explained fixing the two Gaussian energies. A preliminary account of the experimental results is presented in the following. In Figure 3, profiles for $Q = (0.5, 0.5, 0.0)$ r.l.u. illustrate the typical renormalization of the $\Gamma_4 \rightarrow \Gamma_5(1,2)$ CEF transition as a function of the temperature. At $T = 2$ K the observed mean excitation energy corresponds to $E = 1.72(1)$ meV with an overall doublet splitting $\delta E = 0.18(1)$ meV. The discussion of the former with respect to the internal exchange mean-field has already been presented, which matches the value $B_{mf} = 3.0$ T as motivated (Fig. 3, inset). Numerical expressions of the relevant model calculations at $B_{mf} = 3.0$ T are reported in Table 1. We comment here on the doublet splitting, which is decidedly larger than calculated, but within instrumental accuracy fixed throughout the reciprocal space. Interestingly, former powder INS investigations also reported the broad nature of the low-lying transition, see references [6,11]. From the novel single crystal INS investigations this is unambiguously ascribed to an intrinsic feature present at each wave vector and not to a powder averaged effect. Within experimental accuracy, the absence of resolvable energy dispersion of the low-lying singlet-doublet transition is in agreement with the same model approach explaining the higher singlet-singlet transitions, albeit implying an intrinsic origin of the doublet splitting δE at the mean-field CEF level. The corrections to equation (6) due to the orthorhombic distortion in the AF phase qualitatively support the increase of the calculated δE against Table 1, but quantitatively underestimate the experimental observations. However, for nearly degenerate states the perturbative model approach in the Appendix possibly bears less confidence and a more involved treatment might prove of advantage. As a further ingredient of the magnetism in $HoNi_2B_2C$ we mention here the underlying superconducting state, see references [4,22] and references therein. The strength of the exchange interactions between the Ho-Ho ions is mediated by the conduction electrons, whose susceptibility is influenced by the superconducting state. Theories predicting a freezing of the the dispersive behavior of the magnon excitations in materials with coexisting superconductivity and antiferromagnetic order are described in reference [23]. These effects are particularly pronounced around $q = 0$ and at the nesting vectors. INS investigations of the phonon excitations in the borocarbides reveal incipient lattice instabilities at the nesting vectors as in references [24–27] and references therein. Along the same lines, the low-lying $\Gamma_4 \rightarrow \Gamma_5(1,2)$ CEF transition is planned to be investigated at fixed $T = 2$ K for selected external fields below, across and above the upper critical field B_c. A complete account of the experimental results in zero field and as a function of the external field will be presented elsewhere.

To sum up, the inelastic neutron scattering investigation of the magnetic excitons in isotopically substituted $HoNi_2^{11}B_2C$ single crystals provides a strong experimental

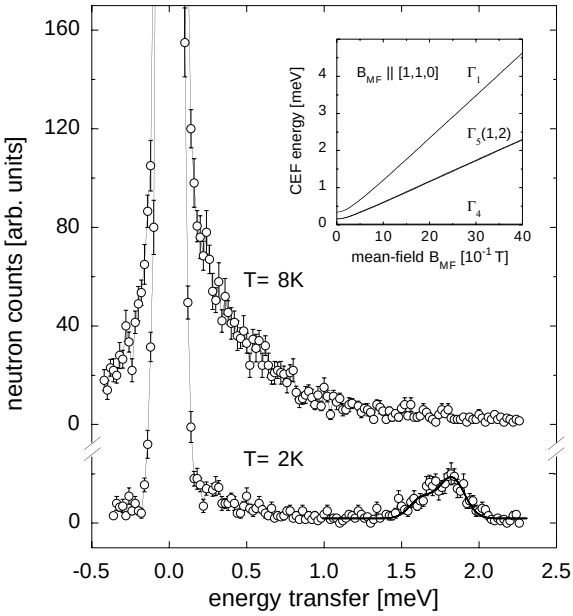

Fig. 3. Neutron profiles of the low-lying $\Gamma_4 \rightarrow \Gamma_5(1,2)$ CEF transition observed in $HoNi_2^{11}B_2C$ single crystals for (0.5,0.5,0.0) r.l.u. at $T = 8$ K $> T_N$ and $T = 2$ K $< T_N$ (DrüchaL, SINQ PSI). The energy renormalization of the transition at $T = 2$ K reflects the exchange mean-field as in the inset, from the calculations explained in the Appendix. The thick continuous line at $T = 2$ K corresponds to the global fit procedure addressed in Section 4.

case which is discussed here for the major CEF transitions. At fixed $T = 2$ K the dynamic exchange interactions remain subordinated to the mean-field CEF interactions, with very weak energy bandwidth around the renormalized CEF energy level. Devoted instrumental configuration and excellent background conditions nevertheless allow the determination of $E(q)$ for the dominant $\Gamma_4 \rightarrow \Gamma_2$ CEF transition. The results successfully capture for the first time the wave vector and energy dependence of the Ho-Ho interactions, completing at the same time previous studies on the subject. The interpretation of the exchange interactions relies on the relative energy change reported around a well-defined CEF transition and is thus regarded as robust. A simple theoretical model with the mean-field consideration of the exchange interactions further indicates self-consistency. It is suggested that the same dynamic framework might apply for the other representatives of the antiferromagnetic and superconducting borocarbides.

5 Conclusions

An investigation of the magnetic excitations in the ordered antiferromagnetic phase of $HoNi_2B_2C$ is reported from inelastic neutron scattering on single crystals. The experiments at fixed $T = 2$ K comprise the main CEF transitions, which for the first time are measured along distinct symmetry directions of the reciprocal space. For

the higher $\Gamma_4 \rightarrow \Gamma_2$, $\Gamma_4 \rightarrow \Gamma_5(2)$ CEF transitions the results indicate very modest and anisotropic energy dispersion, which is almost limited to the plane perpendicular to the $[0,0,1]$ direction. Energy and spectral weight of the observed neutron profiles are compared to model predictions self-consistently developed on the basis of the $J = 8$ ground state multiplet of Ho^{3+} in an effective mean-field. Overall agreement between experiment and theory is claimed considering the simple nature of the model approach. The direct determination of the exchange mean-field from the observed energy bandwidth well compares to previous investigations. The clear advantage of inelastic neutron scattering on single crystals is the selective access to the distinct exchange contributions. The results reveal the importance of next-nearest neighbor interactions in the plane, stressing the complexity of the exchange interactions. For the low-lying $\Gamma_4 \rightarrow \Gamma_5(1,2)$ CEF transition, at each wave vector a broadening of the neutron profiles is reported. The broadening is well described assuming an intrinsic and nondispersive splitting of the doublet excited state. It is hoped that the present investigation will trigger additional efforts towards a better understanding of the magnetic excitations in the borocarbide family.

Fruitful discussions with A. Furrer, D. Petitgrand and S. Raymond are appreciated. The technical support of Ph. Boutrouille during the 4F2 measurement is gratefully acknowledged. This work was financially supported by the Swiss National Science Foundation.

Appendix

The calculation of the neutron cross section relies on the Random Phase Approximation (RPA) model of the $J = 8$ ground state multiplet of Ho^{3+} in the exchange mean-field of the neighbors, see reference [28] for a general discussion. Relevant microscopic information is provided by the the paramagnetic CEF energy scheme determined in reference [6]. The according parametrization of the CEF Hamiltonian reads

$$H_{CEF} = B_2^0 O_2^0 + B_4^0 O_4^0 + B_4^4 O_4^4 + B_6^0 O_6^0 + B_6^4 O_6^4 \quad (6)$$

where the B_n^m are CEF parameters and the O_n^m the Stevens operators. The former are obtained according to the parametrization

$$B_2^m = \alpha A_2^m,\ B_4^m = \beta A_4^m,\ B_6^m = \gamma A_6^m \quad (7)$$

where α, β, γ denote the Stevens' multiplicative factor for Ho^{3+}, and $A_2^0 = -14.5 \pm 6.0, A_4^0 = 2.3 \pm 0.8, A_4^4 = -71.4 \pm 3.3, A_6^0 = -0.42 \pm 0.3, A_6^4 = 11.7 \pm 1.4$ meV. Equation (6) disregards the additional CEF parameters arising from the magneto-restriction in the ordered AF phase, as introduced in Section 2 after references [13,14]. The tetragonal to orthorhombic distortion generally implies nine instead of five independent CEF parameters, see reference [29]. From the point charge model detailed in reference [6], very modest corrections on the scale of the original CEF parameters are estimated under explicit consideration of the 0.19% distortion along the $[1,1,0]$ direction after reference [13]. The additional CEF parameters never exceed a few percent of the dominant B_n^m within each of the $n = 2, 4, 6$ subsets of equation (7). These modest corrections to equation (6) are largely overcome by the renormalization due to the exchange mean-field in equation (1), see also Figure 3 (inset).

Since dealing with a three-dimensional, large spin case the exchange mean-field approximation is adopted as a starting point in the interpretation of the collective exchange interactions. The resulting Hamiltonian $H_{CEF} + H_{MF}$ from equation (6) and equation (1) yields the renormalized energy scheme summarized in Table 1 and further applied in the data analysis. For the purpose of the calculation, the strength of the exchange mean-field $B_{MF} \parallel [1,1,0]$ is fixed at 3.0 T according to the explanations given in the text. The numerical diagonalization is performed in the complete $2J + 1$ spin space of the $J = 8$ ground state multiplet, but disregards higher multiplets. Variances in the determination of the renormalized CEF states are estimated from a homogeneous discretization of the error vector in 5^5 points within the limits given in reference [6], see Table 1. For the low-lying $\Gamma_4 \rightarrow \Gamma_5(1,2)$ singlet-doublet transition, the corrections from the magneto-restriction are separately mentioned in the context of the relative energy splitting of the doublet state, see Section 4. For the higher $\Gamma_4 \rightarrow \Gamma_2$, $\Gamma_4 \rightarrow \Gamma_5(2)$ singlet-singlet transitions, the same are negligible compared with the original variances. Justified by the experimental outcomes, we accordingly neglect the corrections to equation (6) in the quantitative discussion of the exchange interactions.

The exchange contributions to equation (1) stem from the Hamiltonian

$$H_{EX} = -\frac{1}{2} \sum_{ij} \tilde{J}_{ij}\ J_i \cdot J_j \quad (8)$$

where the indexes i, j denote the rare-earth sites and $\tilde{J}_{ij}$ the corresponding interaction. Progressively developing equation (8) in terms of the FT of the planar rare-earth sites yields

$$\tilde{J}(q) = 2\tilde{J}_1 \left(\cos(2\pi q_h) + \cos(2\pi q_k)\right) + 4\tilde{J}_2 \cos(2\pi q_h) \times \cos(2\pi q_k) + 2\tilde{J}_3 \left(\cos(4\pi q_h) + \cos(4\pi q_k)\right) + \ldots \quad (9)$$

The full dynamic spin susceptibility is obtained from the expression

$$\chi(Q,\omega) = \frac{\chi_0(\omega)}{1 - \tilde{J}(q)\chi_0(\omega)} \quad (10)$$

where $\chi_0(\omega)$ is determined from $H_{CEF} + H_{MF}$ as before. In Figure 4, the self-consistent condition of the mean-field approach implying $g\mu_B B_{mf} = \langle J \rangle\ \tilde{J}(q_{AF})$ is illustrated for $g = 1.25$, $\langle J \rangle = 8$. Experimental results in accordance with Figure 4 are discussed in Section 4. The imaginary

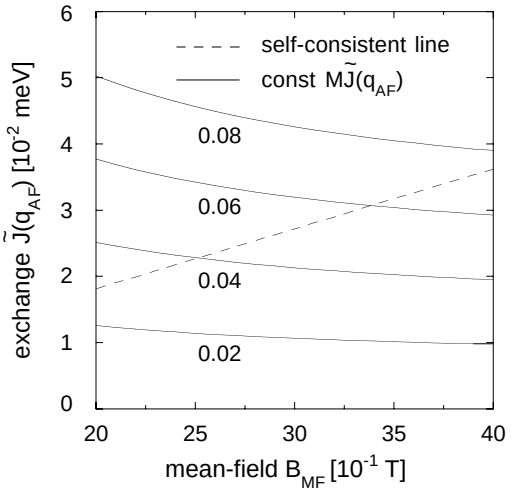

Fig. 4. Illustration of the self-consistent mean-field condition addressed in Section 4. Continuous lines for the $\Gamma_4 \rightarrow \Gamma_2$ CEF transition reproduce different mean-fields B_{MF} at constant $M\tilde{J}(q_{AF})$ values, where $M = M(B_{MF})$. Enforcement of the self-consistent mean-field condition between B_{MF} and $\tilde{J}(q_{AF})$ yields the dashed line. The notation is explained in the text, details of the calculations are presented in the Appendix.

part $\chi''(Q,\omega)$ of the complex spin susceptibility in equation (10) directly enters the INS cross section according to

$$\frac{\mathrm{d}^2\sigma}{\mathrm{d}\Omega \mathrm{d}\omega}(Q,\omega) \sim \frac{Q_f}{Q_i}\ |f(Q)|^2 \sum_{\alpha\beta}\left(\delta^{\alpha\beta} - \frac{Q^\alpha Q^\beta}{Q^2}\right)\ \chi''(Q,\omega) \tag{11}$$

in a notation already introduced, with Q_f and Q_i the final and initial wave vectors, respectively. Linearized expressions restricted to the diagonal matrix elements of this calculation are summarized in Section 3. Though full consideration of the off-diagonal matrix elements is possible, analytical expressions quickly loose their intuitive interpretation without adding definitive insights into the dynamics accessible on an experimental level. Data did not warrant such improvements and we thus remain at the model stage adopted in the discussion of the experimental results. The planned INS experiments at finite external fields as anticipated in the text will hopefully trigger additional interest in the dynamic modeling of the antiferromagnetic phase of $HoNi_2B_2C$.

References

1. K.H. Müller, V.N. Narozhnyi, Rep. Prog. Phys. **64**, 943 (2001)
2. Q. Huang, A. Santoro, T.E. Grigereit, J.W. Lynn, R.J. Cava, J.J. Krajewski, W.F. Peck Jr., Phys. Rev. B **51**, 3701 (1995)
3. J.W. Lynn, S. Skanthakumar, Q. Huang, S.K. Sinha, Z. Hossain, L.C. Gupta, R. Nagarajan, C. Godart, Phys. Rev. B **55**, 6584 (1997)
4. P.C. Canfield, B.K. Cho, D.C. Johnston, D.K. Finnemore, M.F. Hundley, Physica C **230**, 397 (1994)
5. B.K. Cho, B.N. Harmon, D.C. Johnston, P.C. Canfield, Phys. Rev. B **53**, 2217 (1996)
6. U. Gasser, P. Allenspach, F. Fauth, W. Henggeler, J. Mesot, A. Furrer, S. Rosenkranz, P. Vorderwisch, M. Buchgeister, Z. Phys. B **101**, 345 (1996)
7. T.E. Grigereit, J.W. Lynn, Q. Huang, A. Santoro, R.J. Cava, J.J. Krajewski, W.F. Peck Jr., Phys. Rev. Lett. **73**, 2756 (1994)
8. A.I. Goldman, C. Stassis, P.C. Canfield, J. Zaretsky, P. Dervenagas, B.K. Cho, D.C. Johnston, B. Sternlieb, Phys. Rev. B **50**, 9668 (1994)
9. J.P. Hill, B.J. Sternlieb, D. Gibbs, C. Detlefs, A.I. Goldman, C. Stassis, P.C. Canfield, B.K. Cho, Phys. Rev. B **53**, 3487 (1996)
10. P.C. Canfield, S.L. Bud'ko, B.K. Cho, A. Lacerda, D. Farrell, E. Johnston-Alperin, V.A. Kalatsky, V.L. Pokrovsky, Phys. Rev. B **55**, 970 (1997)
11. M. Rotter, C. Sierks, M. Loewenhaupt, J. Freudenberger, H. Schober, in *Rare Earth Transition Metal Borocarbides (Nitrides)*, edited by K.H. Müller, V.N. Narozhnyi (Dordrecht, Kluwer, 2001)
12. U. Gasser, P. Allenspach, in *Rare Earth Transition Metal Borocarbides (Nitrides)*, edited by K.H. Müller, V.N. Narozhnyi (Dordrecht, Kluwer, 2001)
13. A. Kreyssig, M. Loewenhaupt, J. Freudenberger, K.H. Müller, C. Ritter, J. Appl. Phys. **85**, 6058 (1999)
14. A. Kreyssig, A. Schneidewind, M. Loewenhaupt, C. Ritter, J. Freudenberger, G. Fuchs, K.H. Müller, in *Rare Earth Transition Metal Borocarbides (Nitrides)*, edited by K.H. Müller, V.N. Narozhnyi (Dordrecht, Kluwer, 2001)
15. A. Amici, P. Thalmeier, Phys. Rev. B **57**, 10684 (1998)
16. A. Amici, P. Thalmeier, P. Fulde, Phys. Rev. Lett. **84**, 1800 (2000)
17. V.A. Kalatsky, V.L. Pokrovsky, Phys. Rev. B **57**, 5485 (1998)
18. C. Detlefs, F. Bourdarot, P. Burlet, P. Dervenagas, S.L. Bud'ko, P.C. Canfield, Phys. Rev. B **61**, R14916 (2000)
19. A.J. Campbell, D.C. McK. Paul, G.J. McIntyre, Phys. Rev. B **61**, 5872 (2000)
20. J.Y. Rhee, X. Wang, B.N. Harmon, Phys. Rev. B **51**, 15585 (1995)
21. B.K. Cho, P.C. Canfield, L.L. Miller, D.C. Johnston, W.P. Beyermann, A. Yatskar, Phys. Rev. B **52**, 3684 (1995)
22. H. Eisaki, H. Takagi, R.J. Cava, B. Batlogg, J.J. Krajewski, W.F. Peck Jr., K. Mizuhashi, J.O. Lee, S. Uchida, Phys. Rev. B **50**, 647 (1994)
23. A.I. Buzdin, JETP Lett. **40**, 956 (1984)
24. P. Dervenagas, M. Bullock, J. Zarestky, P. Canfield, B.K. Cho, B. Harmon, A.I. Goldman, C. Stassis, Phys. Rev. B **52**, R9839 (1995)
25. H. Kawano, H. Yoshizawa, H. Takeya, K. Kadowaki, Phys. Rev. Lett. **77**, 4628 (1996)
26. C. Stassis, M. Bullock, J. Zarestky, P. Canfield, A.I. Goldman, G. Shirane, S.M. Shapiro, Phys. Rev. B **55**, R8678 (1997)
27. M. Bullock, J. Zarestky, C. Stassis, A. Goldman, P. Canfield, Z. Honda, G. Shirane, S.M. Shapiro, Phys. Rev. B **57**, 7916 (1998)
28. J. Jensen, A.R. Mackintosh, *Rare Earth Magnetism, Structure and Excitations* (Clarendon Press, Oxford 1991)
29. U. Walter, J. Phys. Chem. Sol. **45**, 401 (1984)